PHYSICAL REVIEW B **84**, 014106 (2011)

Positron annihilation in Cr, Cu, and Au layers embedded in Al and quantum confinement of positrons in Au clusters

Philip Pikart[*] and Christoph Hugenschmidt
Physics Department E 21 and FRM II, Technische Universität München, D-85747 Garching, Germany

Michael Horisberger
PSI, Laboratory for Developments and Methods, CH-5232 Villingen PSI, Switzerland

Yoshitaka Matsukawa, Masahiko Hatakeyama, Takeshi Toyama, and Yasuyoshi Nagai
IMR, Tohoku University, 2145-2 Oarai, Ibaraki, Japan

(Received 17 July 2010; published 21 July 2011)

Defect-sensitive and element-selective measurements on ultrathin chrome, copper, and gold layers embedded in aluminium are presented using coincident Doppler broadening spectroscopy (CDBS) with a monoenergetic positron beam. The amounts of positrons implanted in the layers of different thicknesses are calculated and compared with the experimentally gained fractions of positrons annihilating in the buried layers. A high sensitivity was already reached at an Au layer of only 2 nm thickness embedded below 200 nm Al, which was attributed to the highly efficient positron trapping in the Au layer and Au clusters. An implantation and diffusion model describes this high sensitivity for positron trapping layers. A quantum-well model of the positron wave function limits the trapping to gold clusters of a radius larger than 0.23 nm. This result was confirmed experimentally and validated with complementary TEM measurements.

DOI: 10.1103/PhysRevB.84.014106 PACS number(s): 73.21.Ac, 78.70.Bj

I. INTRODUCTION

Open-volume lattice defects and their chemical surrounding can be studied nondestructively by coincident Doppler broadening spectroscopy (CDBS) of the positron annihilation line. Not only vacancies can trap positrons; also agglomerations of atoms with a higher relative positron affinity $\Delta A^+ < 0$ (by definition, the negative sign specifies an attractive potential) form a trapping potential for positrons if the size of the agglomeration and the affinity difference ΔA^+ are appropriate. Therefore, due to its elemental selectivity CDBS is particularly suited to detect small metallic clusters or precipitates embedded in a matrix. In addition, the application of a monoenergetic positron beam allows one to adjust the positron implantation depth which leads to a greatly enhanced sensitivity in a selected depth. For this reason, vacancy-like defects and precipitates in the near surface region of up to a few μm as well as layered systems can be measured.

In the recorded CDB spectra not only the defect density but also the fingerprint of the elements participating in the annihilation process and hence the chemical surrounding of the annihilation site becomes visible.[1–5] For example, CDBS was applied to investigate defects of ion-implanted semiconductors[6] or irradiation-induced defects of Mg-based alloys.[7] In addition, CDBS allows one not only to study the chemical surrounding of defect sites but also to identify agglomerations such as metallic precipitates in alloys, e.g., the formation of Cu precipitates in reactor pressure vessel steels.[8,9] For the investigation of layered samples, thin films, or multilayers, conventional β^+ sources cannot be applied. For these studies, the use of a monoenergetic positron beam is required since the implantation profile can be adjusted by setting the positron implantation energy. We applied this technique first to Al-covered polymer samples[10] and then to buried (ultra-) thin Sn layers in Al.[11,12] In the latter experiment we have demonstrated that even a 0.1 nm layer of tin covered by 200 nm of aluminium was still detectable.[11] The extremely high sensitivity to observe such a low amount of Sn was explained by efficient trapping due to the highly attractive positron affinity of Sn compared to Al.[13] Subsequent calculation showed that in this system Sn clusters of subnanometer size in Al lead to a confinement of the positron wave function.

The present measurement of layered metallic systems shows three advantages over positron measurements on bulk binary alloys. First, by choosing the thickness of the intermediate layer, the size of the embedded structure can be controlled. Second, the targeted implantation of the monoenergetic positron beam at the intermediate layer maximizes the trapping probability there and thus minimizes influences from the surface or the substrate of the layer. Third, in the present study we extended our investigation to embedded metallic layers with elements of highly different positron affinities. Consequently, the interfaces of the layer to the Al matrix are expected to form an attractive well which amounts to -1.82 eV for Au and -0.06 eV for Cu or even a repulsive potential of $+1.58$ eV at the Cr layers (see Table I). The purpose of this experiment is the systematic examination of different materials and of different layer thicknesses to experimentally study the trapping probability and in particular its correlation to the structure size of the embedded layer. These properties are difficult to calculate due to the high number of concurring processes of the positron in the sample like trapping in open volume defects, in agglomerations, or in phases of various alloys.

The measurements on metallic layered systems show a reliable way to determine the critical size r_c of clusters, which

TABLE I. Characteristics of the used elements: Layers of Au, Cu, and Cr are buried in the Al matrix. The lattice mismatch Δa is calculated from the lattice constants a of the respective bulk material by $\Delta a = a_{\text{layer}}/a_{\text{Al}} - 1$. The positron affinity A^+ is calculated from the work functions of the positron and the electron (experimental values from Coleman, Ref. [15]). The relative positron affinity is defined as $\Delta A^+ = A^+_{\text{layer}} - A^+_{\text{Al}}$. Negative values of ΔA^+ indicate an attractive potential for positrons.

Element	a (nm)	Δa (%)	A^+ (eV)	ΔA^+ (eV)
Al	0.405	0	−4.28	0
Au	0.408	+0.7	−6.1	−1.82
Cu	0.361	−10.8	−4.34	−0.06
Cr	0.291	−28.1	−2.7	+1.58

is important, e.g., for the quantitative evaluation of CDBS measurements on precipitation growth.

II. EXPERIMENT

A. (Coincident) Doppler broadening spectroscopy and positron affinity

After implantation, positrons thermalize within picoseconds, diffuse through the crystal lattice (in the range of 100 nm), and finally annihilate with an electron of the sample. The annihilation process is dominated by the decay into two photons—of exactly 511 keV each—in the center-of-mass system of electron and positron. Since the energy of the fully thermalized positron can be neglected, the momentum of the electron-positron system is determined mainly by the electron momentum. Hence, the shape of the Doppler-broadened annihilation line is a direct indicator of the electron momentum distribution at the annihilation site (see, e.g., Schulz and Lynn[14]). The annihilation occurs either from the delocalized Bloch state, or the positron annihilates from a trapped state in the attractive potential formed by a vacancy-type defect or by a precipitate with higher positron affinity. According to the Fermi energies in metals the annihilation of conduction electrons typically leads to a Doppler-shift of up to 2 keV, whereas the high momentum of the core electrons causes larger Doppler shifts. If the positron is trapped in open-volume defects such as vacancies, the annihilation probability with core electrons strongly decreases, which leads to a lower photon intensity in the high-momentum region and hence to a narrowing of the annihilation line. Due to the high sensitivity for defects, this effect is usually measured by conventional Doppler broadening spectroscopy (DBS) using a single high-purity Ge detector.

When both annihilation photons are detected in coincidence by a collinear setup of two Ge detectors, more detailed information about the annihilation site can be gained. The probability density of the positron has a small overlap with strongly bound core electrons of the sample, which carry high momenta and whose momentum distribution is element specific. These accordingly rare events in the outer tail of the annihilation line can precisely be recorded if the gamma background is reduced to a signal-to-noise ratio of better than 10^5 using two detectors in coincidence to detect the sum energy of 1022 keV of both emitted photons (see, e.g., Hugenschmidt[11]). Consequently, CDBS reveals the contribution to the annihilation line of electrons from different elements by analyzing the photon intensity in the high-momentum region, i.e., at large Doppler shifts, of the recorded spectra.

Not only vacancy-like defects form attractive potentials for positrons but also metallic clusters or layers as long as their positron affinity is higher than the surrounding material. The reason for this effect is the potential step formed at the interface of two materials A and B. The according energy difference ΔE is defined by the chemical potentials of the positron and the electron $\mu^\pm$ in each material and the interface dipole $D_{AB} = \mu_A^- - \mu_B^-$: $\Delta E = \mu_A^+ - \mu_B^+ + D_{AB}$. This equation can be rewritten using the definition of the positron affinity $A^+ = \mu^+ - \mu^-$ and the relation $\Phi^\pm = -\mu^\pm \mp D_0$, where $\Phi^\pm$ are the work functions of the positron and of the electron, respectively. Since the dipole barriers at the surface D_0 and at the interface D_{AB} are respectively the same for electrons and for positrons but with opposite sign one obtains finally $\Delta E = A_A^+ - A_B^+ \equiv \Delta A^+$.[13] Since the more negative values for A^+ correspond to higher positron affinity, in this work $\Delta A^+ < 0$ denotes an attractive potential for positrons.

The positron affinities A^+ and the differences with respect to Al ΔA^+ were calculated from the experimentally determined values for Φ^+ and Φ^- given by Coleman[15] and are listed in Table I. If multiple data were available as in the case of Al and Cu, A^+ was averaged for different crystallographic orientations. Assuming spherical clusters of the respective elements embedded in the Al matrix one can calculate its minimum size with the critical radius r_c that is necessary to form a bound state of the positron inside. According to the definition given above for $\Delta A^+ < 0$, r_c can be calculated in units of the Bohr radius a_0 by $r_c \cong 5.8 \times a_0/\sqrt{|\Delta A^+|/[\text{eV}]}$.[13]

B. CDB spectrometer at NEPOMUC

For the present experiment, the CDB spectrometer at the high intensity positron source NEPOMUC (NEutron induced POsitron source MUniCh) at the research reactor FRM II of the Technische Universität München (TUM) was used.[16] The positron intensity at the sample was set to 2×10^6 positrons per second according to a single count rate of 4×10^4 counts per second in the Ge detectors while the energy resolution is kept at 1.35 keV at $E = 511$ keV. The beam diameter is about 300 μm which enables lateral scanning over the sample (not used for this study). Fast preamplifiers and digital signal processing modules (Canberra) for data acquisition are applied. The diagonal geometry of the detector setup[17] minimizes self-absorption of the annihilation radiation in the sample, and therefore, a coincident count rate of up to 620 events per second in the projection area of the annihilation photo peak is achieved. The measurement time amounts to 6 h per spectrum resulting in typically 1.3×10^7 coincident counts in the 511 keV photo peak.

C. Calculation of the positron implantation profiles

The positron implantation profile in materials can be approximated by Makhovian functions with high precision.[18] Figure 1 exemplarily shows implantation profiles calculated

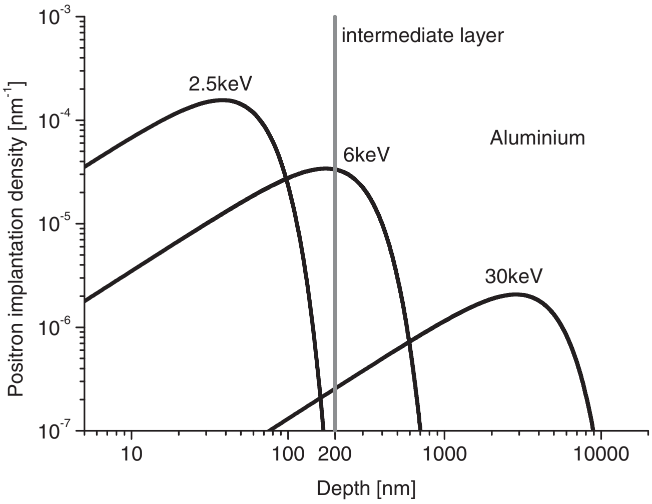

FIG. 1. Implantation profiles of positrons in pure Al approximated by Makhovian functions (material parameters from Ref. 18).

for three different positron energies in Al. It can be clearly seen that a positron beam of 6 keV is well suited to study thin layers embedded below 200 nm Al. Hence, highest sensitivity to reveal information of the embedded layer at this depth is expected at medium energies like 6 keV where the overlap of the positron implantation profile with the intermediate layer is maximized. At 2.5 keV the positrons are implanted nearly completely in the cover layer of 200 nm whereas at 30 keV almost all positrons thermalize in the substrate. Consequently, by adjusting the positron implantation energy, results from CDBS can be gained for the cover layer, for the intermediate region, and for the substrate.

Figure 2 shows the implantation profile calculated for a 6 keV positron beam in a 100 nm thick layer of Au embedded in Al. The high peak at the Au layer is attributed to the high density and high nuclear charge Z which result in high positron stopping power of Au. It was calculated that a fraction $f = 62.2\%$ of the positrons are directly implanted into the Au layer, and the other fraction is implanted near the Al-Au interface. The fractions f of positrons implanted in the embedded layer were calculated for all samples and are summarized in Table II. The required Makhov parameters for Al, Cu, and Au are taken from Puska.[18] Since no experimental values for Cr have been reported so far, the required parameters have been well approximated by linear interpolations as a function of the mass density. Vehannen[19] shows that a modified Makhovian function fairly represents the implantation in a layered system. If $P_x(z)$ represents the transmission probability function for a positron in a material x then a transmission probability function can be defined piecewise for a layered system according to Table III. The implantation density $I(z) = \frac{\partial P(z)}{\partial z}$ is defined as the derivate of the transmission probability. Figure 2 shows the calculated implantation profile for the layered system with a gold layer of 100 nm thickness.

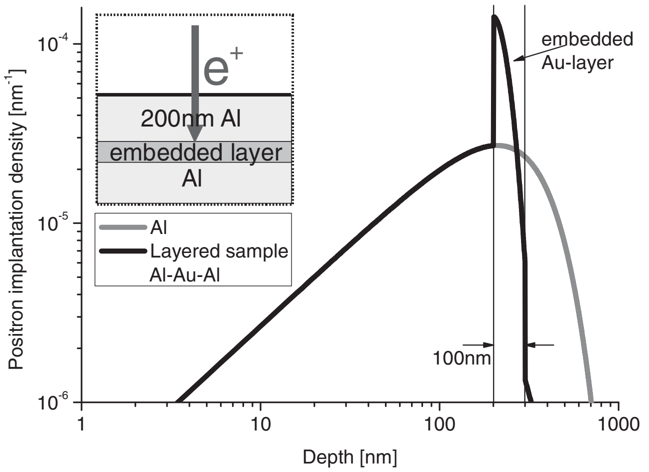

FIG. 2. The implantation profile of a 6 keV positron beam in a 100 nm thick layer of Au embedded in Al (sample 3) compared with the profile for pure Al.

D. Sample preparation

The general structure of the investigated samples is shown in Fig. 2. The substrate consists of annealed Al of 1 mm thickness. Hence, even at a positron energy of 30 keV according to a mean positron implantation depth of 4.0 μm, no positron can reach the bottom. The layers according to Table II are grown by magnetron sputtering out of high-purity materials. Magnetron sputtering produces films of comparatively high densities, i.e., samples with a low amount of free volume.[20] Complementary scanning electron microscope (SEM) measurements assured the quality of the samples. Vertical cuts have been performed with a focused ion beam and have been examined by SEM. The SEM images show the polycrystalline structure of the intermediate and cover layer, while the crystallites of the annealed substrate are too large to be visible in the image dimensions. As an example, the SEM image of sample 7 is shown in Fig. 3. The rough structure of the sample surface, which is visible above the cutting edge, is a side effect of the ion-beam cutting.

III. MEASUREMENTS AND RESULTS

A. Reference spectra and energy-dependent CDBS

First, CDB measurements on reference samples of annealed, high-purity materials (Al, Au, Cr, and Cu) were

TABLE II. The layered samples: The thickness of the layer consisting of the listed element embedded in Al is denoted with d. The cover layer at all samples is 200 nm Al. The calculated fraction of positrons implanted into the layer with a positron beam of 6 keV energy is f. The experimentally obtained values of η reflect the relative portion of positrons annihilating with electrons from elements of the layer.

Sample	Element	d (nm)	f	η
1	Au	0.5	0.006	0
2	Au	2	0.024	0.83
3	Au	100	0.622	0.92
4	Cu	10	0.081	0
5	Cu	100	0.561	0.88
6	Cr	10	0.087	0
7	Cr	100	0.574	0

TABLE III. The sections of the transmission probability function for a layered system of Al substrate, an intermediate layer of material x and thickness d, and a covering layer of $d_0 = 200$ nm Al. s_1 and s_2 have to be solved to fulfill the continuity conditions.

Layer	Depth	Function
Covering layer	$z \leqslant d_0$	$P_{\mathrm{Al}}(z)$
Intermediate layer	$d_0 < z \leqslant d_0 + d$	$P_x(z + s_1)$
Substrate	$d_0 + d < z$	$P_{\mathrm{Al}}(z + s_2)$
Continuity condition 1		$P_{\mathrm{Al}}(d_0) = P_x(d_0 + s_1)$
Continuity condition 2		$P_x(d_0 + d + s_1) = P_{\mathrm{Al}}(d_0 + d + s_2)$

performed. The recorded spectra of the annihilation lines are normalized to equal integral number of counts and mirrored at the symmetry axis at 511 keV to enhance the statistics. Then, the spectra are divided by the Al reference spectrum which hence forms the baseline of the plotted graph. The resulting spectra are called *ratio curves* wherein the differences in the shape of the Doppler-broadened peak become clearly visible to the eye, and the element-specific signature is revealed (see Fig. 4).

Due to the high positron annihilation probability of 11.3% with the electrons of the $3p$ orbital of Cr[21], the photon intensity at high Doppler shifts around 516 keV according to the electron momentum of $20 \times 10^{-3} m_0 c$ is among the highest which has been measured so far. The high electron momentum of Cu results from annihilation with electrons from the $3s$ and $3p$ orbitals, and the signature of Au is mainly attributed to annihilation of $5s$ and $5d$ electrons.

Energy-dependent CDB measurements on sample 2 with the 2 nm Au layer embedded in Al were performed in order to confirm the calculated implantation profiles. The according ratio curves obtained for a positron energy of 2.5, 6, and 30 keV are shown in Fig. 5. At 6 keV the Au layer is clearly visible due to the targeted positron implantation in the layer's depth. At 2.5 keV the positrons are implanted near the surface in the cover layer according to Fig. 1. At 30 keV almost all positrons are implanted in the Al substrate at a mean depth of 4 μm. In contrast to the implantation at 6 keV no Au signature is revealed at 2.5 and 30 keV implantation energy. Consequently, the results confirm the implantation calculations and clearly demonstrate the advantages of using a monoenergetic positron beam and thin layered systems.

B. Layers of Cr, Cu, and Au embedded in Al

The ratio curves obtained by CDBS for all layered samples are presented in Fig. 6. Figure 6(a) shows the spectra of the samples with Cr layers embedded in Al (samples 6 and 7). As expected due to the repulsive positron affinity of Cr in Al the 10 nm layer is not visible in the spectrum. Even the measurement in the 100 nm layer revealed no significant contribution of the pronounced Cr signature, although according to the Makhov calculations 57.4% of the positrons are implanted in the layer.

In Fig. 6(b) the results of two embedded Cu layers with different thickness are presented (samples 4 and 5). The 100 nm layer, in which 56.1% of the positrons are implanted, creates a clearly visible Cu signature, whereas the spectrum of

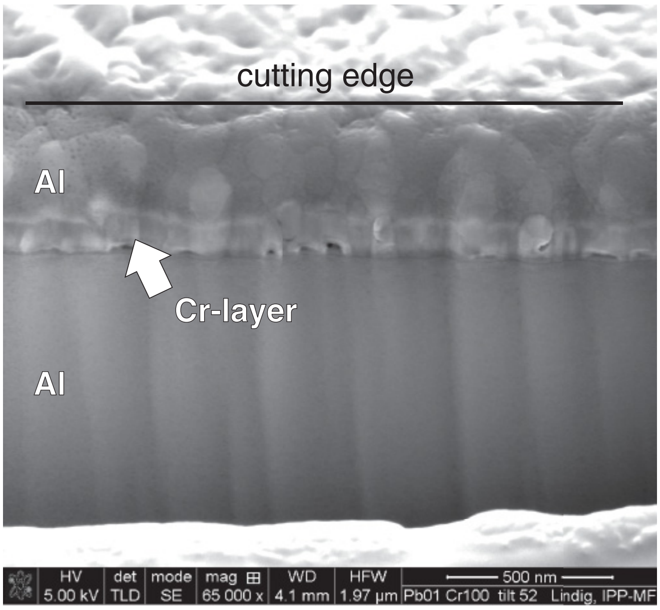

FIG. 3. An electron microscopic (SEM) image of the focused ion beam (FIB) prepared sample with a 100 nm Cr layer embedded in Al (sample 7).

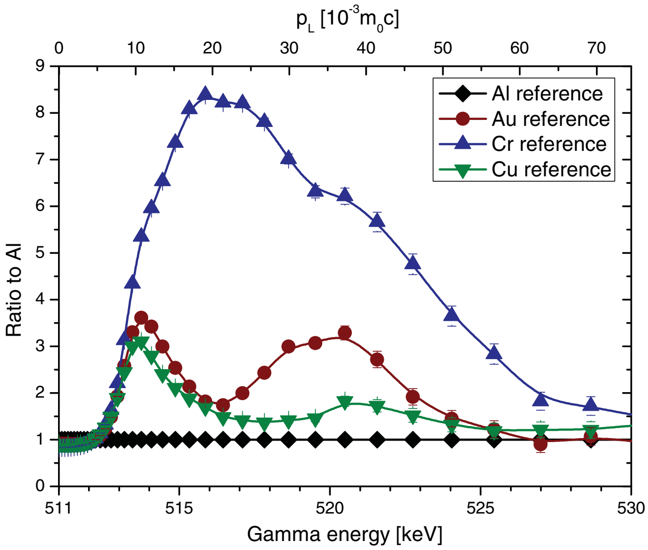

FIG. 4. (Color online) CDBS results of the pure reference materials. All recorded spectra were divided by the spectrum of pure Al to show the element specific shapes as clearly distinguishable *ratio curves*. The lines in all CDB spectra presented in this paper are plotted to guide the eye.

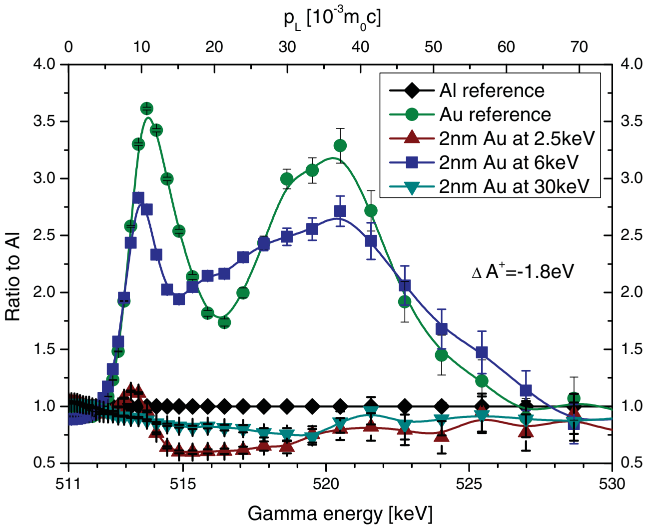

FIG. 5. (Color online) CDBS at different positron implantation energies on sample 2 with a 2 nm Au layer embedded in Al. The large overlap of the positron implantation profile at 6 keV with the embedded Au layer leads to a clearly observable Au signature.

the 10 nm Cu layer is similar to that observed at the thin Cr layer.

The ratio curves for three different embedded Au layers (samples 1–3) are shown in Fig. 6(c). Due to the highly attractive positron affinity of Au in Al, a clear Au signature at the 100 nm layer was recorded which remained almost the same even at the 2 nm layer. A further sample with an embedded Au layer with only 0.5 nm showed no Au signature at all.

Before the reasons for this strongly nonlinear behavior are discussed in Sec. IV, the amount of positrons, which annihilate in the embedded layer, is quantified. For this purpose, least-squares error fits have been applied to the recorded spectra according to the previously performed experiments on Sn layers embedded in Al.[11] The fitting range was limited to the high-momentum area between 513.5 keV and 525 keV to minimize the influence of conduction electrons with momenta below $10 \times 10^{-3} m_0 c$ and background events at electron momenta higher than $55 \times 10^{-3} m_0 c$. The fitting function $I_{\mathrm{fit}}(E)$ is composed of a linear combination of the measured CDB spectra obtained for the respective pure elements $I_x(E)$ ($x =$ Cr, Cu, and Au) and $I_{\mathrm{Al}}(E)$: $I_{\mathrm{fit}}(E) = (1-\eta) I_{\mathrm{Al}}(E) + \eta \times I_x(E)$. The only free fitting parameter η reflects the fraction of positrons annihilating with electrons from the element of the embedded layer. If positron annihilation would only occur inside defect free layers and agglomerations of the used elements, the fit would agree with the data within the statistical error. However, defects due to the lattice mismatch and due to the grain boundaries would lead to a deviation of the measured spectrum of the layered sample from the linear combination of the pure reference spectra.[22]

The resulting values for η obtained from the CDBS measurements are compared with the calculated fractions of positrons implanted in the embedded layer f and summarized in Table II. For samples 1, 4, 6, and 7 no minimum in the square error function for $0 < \eta < 1$ could be found. Thus, at these samples no signature of the embedded elements is observed; i.e., the embedded layer of these samples was not detectable by CDBS.

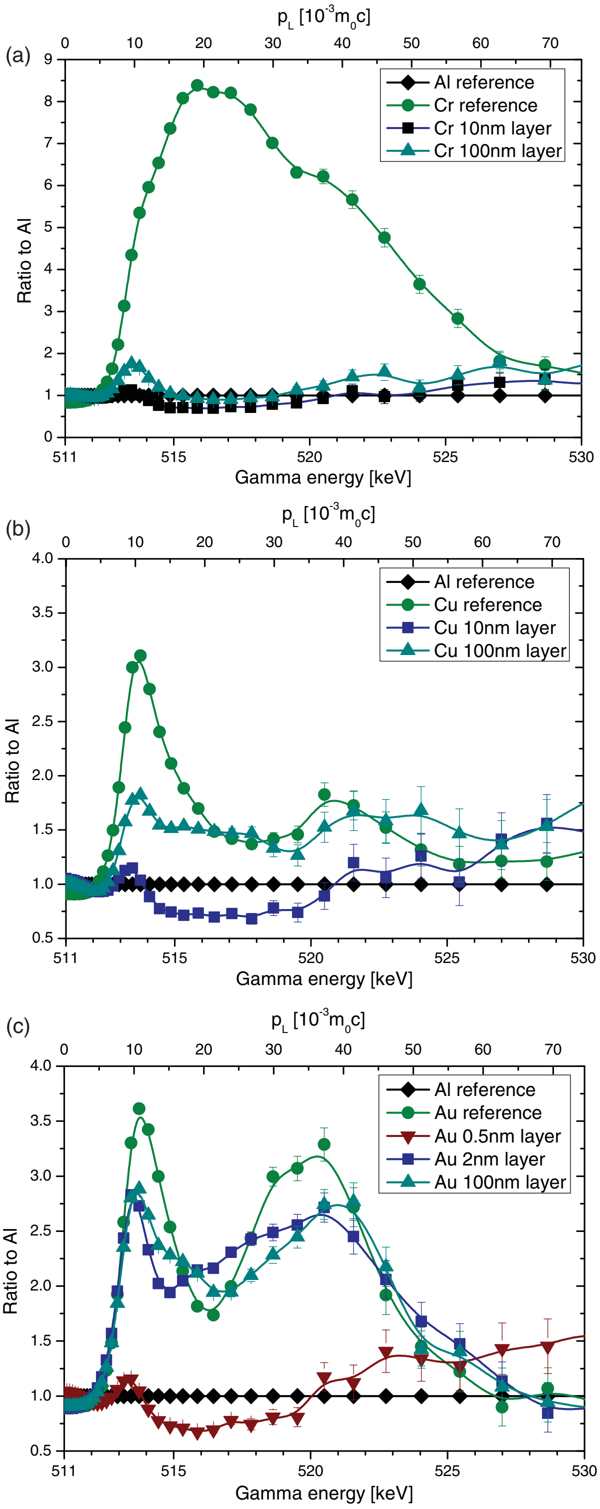

FIG. 6. (Color online) Ratio curves of metallic layers of different thicknesses embedded in Al: Cr in Al (a), Cu in Al (b), and Au in Al (c). The respective reference spectra of the pure elements are plotted as well. Note the different relative positron affinity ΔA^+ of the layered systems (see Table I).

C. Complementary TEM measurements

The astonishing high sensitivity of the CDBS measurement to the 2 nm thin gold layer is explained by an efficient trapping of the positrons at the intermediate layer. Though the high trapping rate can be easily explained by positron confinement due to an attractive positron affinity difference, the positron has to move from its implantation site to the intermediate layer by thermal diffusion. To understand the diffusion process, it is necessary to know the structure of the trapping layer. For this reason, transmission electron microscope (TEM) pictures have been taken of this particular sample. The sample was prepared by conventional FIB lift-out technique. The multilayers are in crosscut view, and they are parallel to the edge of the wedge-shaped TEM specimen. The FIB machine and the TEM of Tohoku University at the IMR, Oarai, Japan, have been used.

Figure 7 shows the essential results of the TEM. The upper image was obtained with no objective lens aperture. The gray-scale contrast in the upper image originates from inelastic scattering primarily dependent on the atomic number and therefore provides information of local chemical composition. Heavier elements exhibit darker contrast. The "Aperture out" image indicates that areas (a) and (c) consist of lighter elements, i.e., aluminium in this case, and the area (b) contains gold. The area (b) exhibits nonuniform contrast, indicating compositional fractionation within the layer. The dark portions are most likely gold precipitates [area (d)] embedded in a gold-aluminium alloy matrix. The average thickness of the alloy is 9 ± 1.5 nm. Because the amount of deposited gold is known from the sample preparation process, the gold concentration in the intermediate layer can be calculated. It amounts up to 66 ± 11 mass percent or 22 ± 3.7 atomic percent.

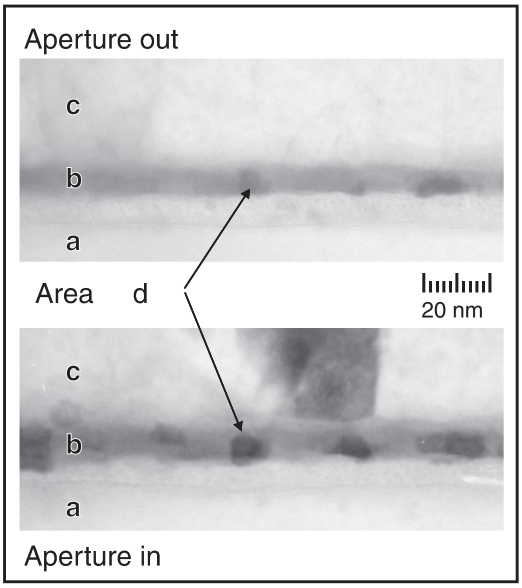

FIG. 7. This TEM picture shows the intermediate layer of the Al sample containing 2 nm gold. Area (a) is identified as the aluminium substrate. Area (b) is the polycrystaline intermediate layer containing gold. Area (c) is the cover layer of pure aluminium. Area (d) shows clusters in the intermediate layer of Au-Al alloy with higher gold concentration. The same area of the sample is imaged with and without the objective lens aperture.

The lower TEM picture ("Aperture in") is a bright-field image that visualizes grains and their boundaries. The substrate shows no grain boundaries at all due to a grain size which is much larger than the field of view. In relation to positron diffusion lengths the substrate is quasi-monocrystalline. The intermediate layer [area (b)] is polycrystalline due to grain boundaries visible right next to the area (d) clusters. The cover layer is polycrystalline with a typical grain size larger than 100 nm. This grain size is in the same order of magnitude than positron diffusion length, so that diffusion along grain boundaries must not be neglected.

In conclusion of the TEM results the layered aluminium gold sample has optimal characteristics for effective positron trapping at the buried layer: The grains are big enough to enable long positron diffusion lengths, and the accordance of the lattice constants, respectively the negligible lattice mismatch of gold and aluminium, minimizes the concentration of open volume defects at the interface.

D. Monte Carlo simulations of thermal positron diffusion

One of the TEM results is the presence of a continuous layer of up to 22 at. % gold content. According to the CDBS results this aluminium gold alloy is apparently able to trap the thermally diffusing positron. In order to explain the efficient positron trapping no detrapping is considered. Here, Monte Carlos simulations can provide an upper limit for the trapping rate at the intermediate layer by the simulation of a three-dimensional random walk which represents the thermal positron diffusion precisely.[19] For trapping at planar layers not the mean diffusion length according to Fick's law and the Einstein-Smoluchowski relation are directly relevant,[23] but it is necessary to know the probability for a positron which is implanted in the depth z to once reach a layer in depth d during the diffusion process. Figure 8 demonstrates that during the

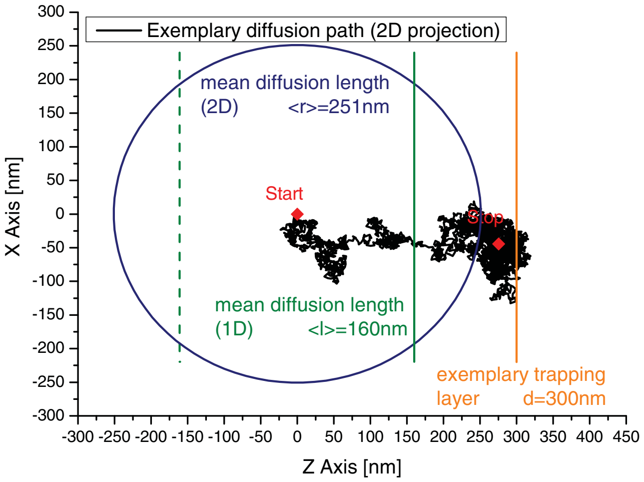

FIG. 8. (Color online) An exemplary three-dimensional random walk projected to two dimensions. A comparatively small mean diffusion length in 1D projection (162 nm) corresponds to a $\approx \frac{\pi}{2}$ longer diffusion length in two dimensions (circle). In this exemplary path the particle reaches the trapping layer in $d = 300$ nm distance to the implantation site.

random walk a layer can be reached which is more distant to the implantation depth than the end point of the free diffusion.

For this study, the influence of positron trapping at the surface or in vacancies is not implemented in the random walk simulation. The necessary parameters $\bar{l}$, the average free path of the positron, and N, the number of scatterings, can be calculated from the diffusion law.[23] The lifetime of the positron is $\tau = 161 \pm 2$ ps,[24] and the diffusion length is $L_+ = 160 \pm 15$ nm.[25] The mean velocity of the positron is $\bar{v} = \sqrt{8k_BT/\pi m}$ and the average free path $\bar{l} = \frac{3D_+}{\sqrt{3k_BT/m}}$ with a diffusion coefficient $D_+ = 1.7\ \text{cm}^2/\text{s}$.[25] Room temperature $T = 300$ K is assumed for all calculations. As a result, the mean free path of the positron is $\bar{l} = 4.37$ nm and the mean number of scatterings is $N = 3964$.

Figure 9 shows the results of the Monte Carlo simulation and their relevance to the measurement of the 2 nm gold layer. From top to bottom, the graphs contain (a) the implantation profile $I(z)$ of the 6 keV positron beam according to the modified Makhovian function (see Sec. II); (b) the result of the Monte Carlo simulation which shows the probability $p(z)$ of a positron which is implanted in a depth z to reach an intermediate layer at $z = 200$ nm; (c) the product $I(z)p(z)$, which shows the part of the implanted positrons which are able to reach the intermediate layer; and (d) the density $\rho_+(z)$, which is calculated from the end points of the Monte Carlo simulation. After the diffusion process, a small ratio of the positrons remains in the aluminium of the sample; 73% ± 3% are trapped in the intermediate layer.

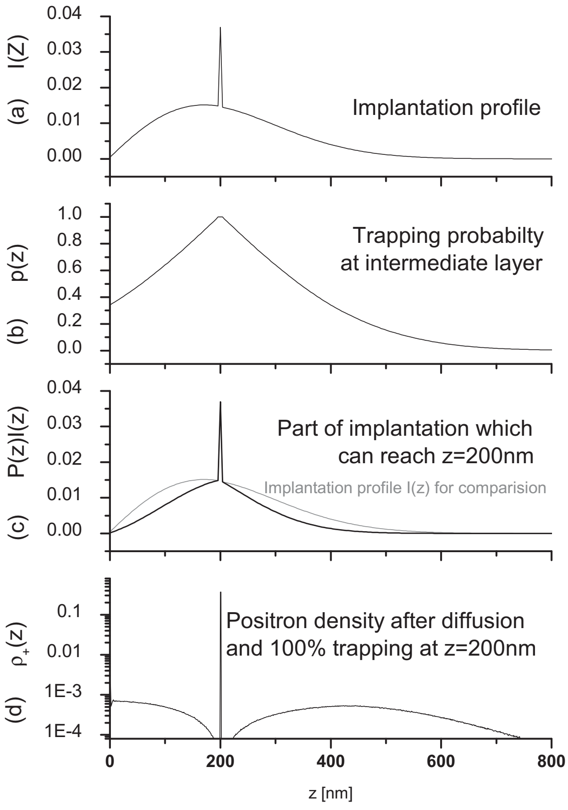

FIG. 9. Sample 2: (a) Implantation profile. (b), (c) Diffusion probabilities. (d) The resulting positron density after diffusion.

The measured value $\eta = 82\%$ of positron annihilation near gold atoms is slightly higher than the calculated maximum trapping ratio of 73% ± 3% although diffusion limiting effects like vacancy or surface trapping are neglected. This deviation can be explained by several reasons: First, the grain boundaries in the covering layer may be contaminated with gold atoms. Vacancies in aluminium are fully mobile at room temperature and, assuming that in the production process vacancies migrated from the intermediate layer to the surface, gold atoms may have diffused into the covering layer as well. Second, the Monte Carlo simulation used isotropic diffusion all over the specimen. But the TEM mesurements clearly showed grain boundaries in the covering layer which are mainly perpendicular to the gold layer and hence could have caused a more directed diffusion to the intermediate layer.

IV. DISCUSSION

A. Positrons in layers

The presented results show a highly nonlinear correlation between the positron affinities, the thickness of the embedded layers, and the element-dependent photon intensities in the high-momentum region of the annihilation line. For the discussion of the results, several aspects have to be considered which influence the shape and the intensity of the CDB spectra. After implantation, thermalized positrons diffuse through the lattice with a diffusion length in the defect free Al of typically 160 nm.[25] Dependent on the concentration on trapping sites such as vacancy-like defects, the diffusion length can be reduced considerably. Both processes play a major role, trapping in open-volume defects and the attraction or repulsion at interfaces due to the element-dependent positron affinities.

Positrons diffusing to the layer's interface are trapped if open-volume defects are present. The number of those defects is expected to be large if the lattice mismatch at the interface is high (see Table I). For positrons trapped in open-volume defects the smaller core annihilation probability would lead to a lower photon intensity in the high electron momentum region than annihilation in the unperturbed lattice. The result of positron annihilation at grain boundaries, which become more important if the grain size is smaller than the positron diffusion length, would be similar. On the other hand, due to the higher positron mobility at the grains' surface the probability to reach the layer-matrix interface would increase which becomes more important if the grain size is on the order of the layer thickness.

The positron affinities A^+ of the materials have to be considered in particular if its difference ΔA^+ is higher than the thermal energy of the positron. For example, an attractive (repulsive) potential barrier is formed at the Al-Au (Al-Cr) interface which attracts (repels) positrons diffusing from the Al matrix to the Au (Cr) layer. In addition, small clusters of a material with strong positron affinity would form positron trapping sites.

B. Defect trapping

For all samples with the thinnest embedded layer—10 nm at Cr and Cu as well as only 0.5 nm of Au—a very similar shape and a lower intensity in the high-momentum region is observed (see Fig. 6). This effect is to the presence of open-volume defects which lead to a reduced core annihilation probability for trapped positrons. For instance, due to the missing repulsive core potential, a single vacancy in Al forms a potential well for positrons of about 1 eV depth.[1]

Even at the thickest Cr layer embedded in Al [Fig. 6(a)], although the Cr signature is very pronounced (see reference in Fig. 4), Cr is not visible and the Cr signature could not be fitted reliably. In this case, trapping in vacancy-like defects in Al and Cr plays a major role, since the concentration of open-volume defects is expected to be particularly high due to the large lattice mismatch of -28% (see Table I). Moreover, due to the high $\Delta A^+ = +1.58$ eV of Cr in Al the Cr-Al interface forms a repulsive potential. For this reason, the diffusion of thermalized positrons from Al into the Cr layer is inhibited and positrons implanted in the Cr layer diffuse into the Al matrix, which is energetically more favorable. Consequently, due to both vacancy-like defects near the Cr-Al interface and the repulsive potential formed by the Cr layer, the Cr signature becomes not visible in the CDB spectra.

The 100 nm Cu layer in Al (sample 5) leads to a measured fraction of positrons annihilating in Cu of $\eta = 88\%$ which is higher than the fraction of implanted positrons in the Cu layer ($f = 56.1\%$). This effect cannot be explained only by open-volume defects related to the lattice mismatch ($\Delta a = -10.8\%$). Although positron detrapping is expected at room temperature due to the shallow potential formed by the Cu layer of $\Delta A^+ = -0.06$ eV, positrons implanted in Cu would barely diffuse into Al. Accordingly, positrons implanted in Al that reach the Al-Cu interface would rather annihilate with electrons from Cu than from Al.

In sample 3, the 100 nm Au layer is clearly visible in the CDB spectrum [Fig. 6(c)] due to the high positron affinity of Au embedded in Al ($\Delta A^+ = -1.82$ eV). The fitting parameter $\eta = 0.92$, which corresponds to the positron fraction annihilating in Au, is considerably higher than the implantation ratio $f = 0.62$. This is a clear indication that positrons diffuse from the Al matrix into the embedded Au layer. In addition, this diffusion process is not hindered by lattice-mismatch-induced defects since the number of those is expected to be negligible due to the very similar lattice constants of Au and Al (see Table I).

C. Quantum confinement

The most astonishing result was obtained for sample 2 with a 2 nm Au layer embedded in Al. At this sample the Au signature is almost as strong as in the spectrum of the sample with the buried 100 nm Au layer (sample 3), although at 0.5 nm Au in Al no Au signature was detected at all. The accordingly very small amount of positrons implanted in the 2 nm Au layer of $f = 2.4\%$ leads to a huge fraction of positrons annihilating in Au of $\eta = 83\%$.

This strong effect can be only explained by very efficient positron trapping into the energetically more favorable Au layer. The results of the Monte Carlo simulation (Sec. III D) support that the Al-Au alloy layer which was analyzed by TEM (Sec. III C) confines the positron diffusion into the 2-dimensional alloy layer. A stable positron trapping only at the clusters of high gold concentration but not in the alloy layer (see Fig. 7) could not sufficiently explain the high trapping rate. The low momentum part of the CDB spectrum shows significant deviations from the gold reference. Studies conducted on copper clusters in iron[22] demonstrate that these deviations can be caused by the positron localization which differs if the positron is localized in pure bulk material, in small clusters or in alloys. Hence the low momentum deviation indicates that annihilation occurs in the alloy or in small clusters.

The high difference of the positron affinity of $\Delta A^+ = -1.82$ eV for this material combination leads to the formation of an attractive potential for positrons. Therefore, thermalized positrons inside the Au layer or in Au clusters are repelled at the Au/Al interface, and positrons diffusing from Al to the Au layer are efficiently trapped inside the Au layer or Au clusters which have been observed by TEM. As shown in Sec. II A the positron wave function will be confined inside an Au cluster with a minimum size; i.e., the well needs a certain extension in order to possess at least one bound positron state. Assuming a spherical Au cluster with $\Delta A^+ = -1.82$ eV its critical radius r_c is calculated to $r_c \cong 0.23$ nm. Thus, 0.46 nm is the minimum extension of the Au cluster to form a bound positron state. By comparison with the lattice constant of Au ($a = 0.408$ nm) the clusters would be at least of the size of a unit cell and hence contain at least 14 Au atoms. Such clusters (see Fig. 7) hence lead to a three-dimensional quantum confinement of the positron wave function. Moreover the Al-Au alloy formed in the Al matrix first acts as a confinement of the positron diffusion and hence the gold rich clusters with a mean distance of typically 20 nm are reached in the subsequent 2-dimensional diffusion process with very high probability. CDBS data cannot finally distinguish whether the annihilation occurs in the layer of lower Au concentration or in the clusters of high Au concentration.

For the same reason, no positron trapping sites are formed by Au at the sample (No. 1) containing 0.5 nm Au where no Au signature at all was observed. Consequently, the evaporated Au layer of only 0.5 nm thickness is expected to form a Au-Al alloy with lower Au amount than the 2 nm Au layer which does not trap positrons. In addition, the maximum radius of possibly formed Au clusters in this layer is smaller than 0.23 nm, which does not lead to the confinement of the positron wave function. Hence positrons get trapped at vacancies and consequently the CDB spectrum looks similar to the spectra obtained for thin copper or chrome layers.

V. CONCLUSION

A series of CDBS measurements were performed on samples with embedded layers of different positron affinities (Cr, Cu, and Au in Al) and various thickness. This systematic investigation using a monoenergetic positron beam revealed a strong nonlinearity in the response of the CDBS measurements due to the variation of the layer thickness with different elements which was attributed to two main effects. First, vacancy-like defects lead to positron trapping at the layer-matrix interface particularly if the lattice mismatch is high. Second, due the difference of the element-dependent positron affinity a potential step is formed at the interface that enhances the positron annihilation with electrons of the elements with higher positron affinity. Moreover, the huge difference of the results obtained for the 0.5 nm and the 2 nm Au layers embedded in Al demonstrates the extremely high sensitivity to small variations of the elemental concentration in the sample. The theoretically calculated positron affinity was proofed to be a profound basis for the understanding of a quantum confinement based model of the positron trapping in Au clusters with a minimum diameter of 0.46 nm surrounded by Al. We succeeded in experimentally determining the conditions and parameters for effective positron trapping at metallic agglomerations. The comparison of the experimental results with the Monte Carlo simulation of a diffusion model indicated a strong positron trapping behavior of the aluminium-gold alloy present in the Al-Au-Al samples. Because the trapping can actually not be reliably predicted by calculations, this result shows the high importance of measurements on layered metallic model systems for further applications of CDBS in material research such as the characterization of age hardenable alloys, which can be hardened by precipitation growth. In these alloys, components of low concentration significantly change in the precipitation growth during heat treatment. Because CDBS measurements can be performed nondestructively and *in situ* during the heat treatment they are expected to be destined for analyzing the early stages of precipitation growth, if quantitative and experimentally confirmed values about diffusion and critical cluster sizes are available.

ACKNOWLEDGMENTS

The authors thank M. Balder from the Max Planck Institute for Plasma Physics in Garching for recording the FIB images. Fruitful discussions with K. Schreckenbach from the TUM are gratefully acknowledged. A short-term scholarship of JSPS enabled a very productive stay of the authors at the IMR of Tohoku University in Oarai, Japan.

---

[*] philip.pikart@frm2.tum.de

[1] K. G. Lynn, J. E. Dickman, W. L. Brown, M. F. Robbins, and E. Bonderup, Phys. Rev. B **20**, 3566 (1979).

[2] P. Asoka-Kumar, M. Alatalo, V. J. Ghosh, A. C. Kruseman, B. Nielsen, and K. G. Lynn, Phys. Rev. Lett. **77**, 2097 (1996).

[3] S. Szpala, P. Asoka-Kumar, B. Nielsen, J. P. Peng, S. Hayakawa, K. G. Lynn, and H.-J. Gossmann, Phys. Rev. B **54**, 4722 (1996).

[4] P. E. Mijnarends, A. C. Kruseman, A. van Veen, H. Schut, and A. Bansil, J. Phys. Condens. Matter **10**, 10383 (1998).

[5] M. K. A. Baranowski, J. Beliczynski, and M. Szuszkiewicz, Nucl. Instrum. Methods Phys. Res., Sect. A **526**, 420 (2004).

[6] M. Fujinami, T. Sawada, and T. Akahane, Radiat. Phys. Chem. **68**, 631 (2003).

[7] M. Stadlbauer, C. Hugenschmidt, K. Schreckenbach, and P. Böni, Phys. Rev. B **76**, 174104 (2007).

[8] Y. Nagai, M. Hasegawa, Z. Tang, A. Hempel, K. Yubuta, T. Shimamura, Y. Kawazoe, A. Kawai, and F. Kano, Phys. Rev. B **61**, 6574 (2000).

[9] Y. Nagai, Z. Tang, M. Hassegawa, T. Kanai, and M. Saneyasu, Phys. Rev. B **63**, 134110 (2001).

[10] C. Hugenschmidt, J. Mayer, and M. Stadlbauer, Radiat. Phys. Chem. **76**, 217 (2007).

[11] C. Hugenschmidt, P. Pikart, M. Stadlbauer, and K. Schreckenbach, Phys. Rev. B **77**, 092105 (2008).

[12] P. Pikart, C. Hugenschmidt, J. Mayer, M. Stadlbauer, and K. Schreckenbach, Appl. Surf. Sci. **255**, 245 (2008).

[13] M. J. Puska, P. Lanki, and R. M. Nieminen, J. Phys. Condens. Matter **1**, 6081 (1989).

[14] P. Schultz and K. Lynn, Rev. Mod. Phys. **60**, 701 (1988).

[15] P. Coleman, *Positron Beams and Their Applications* (World Scientific, 2000).

[16] C. Hugenschmidt, K. Schreckenbach, M. Stadlbauer, and B. Straßer, Nucl. Instrum. Methods Phys. Res., Sect. A **554**, 384 (2005).

[17] M. Stadlbauer, C. Hugenschmidt, and K. Schreckenbach, Appl. Surf. Sci. **255**, 136 (2008).

[18] M. Puska and R. Nieminen, Rev. Mod. Phys. **66**, 841 (1994).

[19] A. Vehanen, K. Saarinen, P. Hautojärvi, and H. Huomo, Phys. Rev. B **35**, 4606 (1987).

[20] H. Garbacz, P. Wiecioski, B. Adamczyk-Cielealak, J. Mizera, and K. Kurzydowski, J. Microsc. **237**, 475 (2010).

[21] K. O. Jensen and A. Weiss, Phys. Rev. B **41**, 3928 (1990).

[22] Z. Tang, T. Toyama, Y. Nagai, K. Inoue, Z. Q. Zhu, and M. Hasegawa, J. Phys. Condens. Matter **20**, 445203 (2008).

[23] H. Mehrer, *Diffusion in Solids*, Springer Series in Solid-State Sciences (Springer, Berlin, 2007), Vol. 155.

[24] T. M. Hall, A. N. Goland, and C. L. Snead, Phys. Rev. B **10**, 3062 (1974).

[25] E. Soininen, H. Huomo, P. A. Huttunen, J. Mäkinen, A. Vehanen, and P. Hautojärvi, Phys. Rev. B **41**, 6227 (1990).